

Near-IR fluorescence and reflectance confocal microscopy for imaging of quantum dots in mammalian skin

Luke J. Mortensen,¹ Christopher E. Glazowski,²
James M. Zavislan,^{1,2,3} and Lisa A. DeLouise^{1,3,*}

¹Department of Biomedical Engineering, University of Rochester, Rochester, New York 14642, USA

²Department of Optics, University of Rochester, Rochester, New York 14642, USA

³Department of Dermatology, University of Rochester, Rochester, New York 14642, USA

*Lisa_DeLouise@urmc.rochester.edu

Abstract: Understanding the skin penetration of nanoparticles (NPs) is an important concern due to the increasing presence of NPs in consumer products, including cosmetics. Technical challenges have slowed progress in evaluating skin barrier and NP factors that contribute to skin penetration risk. To limit sampling error and other problems associated with histological processing, many researchers are implementing whole tissue confocal or multiphoton microscopies. This work introduces a fluorescence and reflectance confocal microscopy system that utilizes near-IR excitation and emission to detect near-IR lead sulfide quantum dots (QDs) through ex vivo human epidermis. We provide a detailed prediction and experimental analysis of QD detection sensitivity and demonstrate detection of QD skin penetration in a barrier disrupted model. The unique properties of near-IR lead-based QDs will enable future studies that examine the impact of further barrier-disrupting agents on skin penetration of QDs and elucidate mechanistic insight into QD tissue interactions at the cellular level.

© 2011 Optical Society of America

OCIS codes: (160.4236) Nanomaterials; (170.1790) Confocal microscopy; (170.3880) Medical and biological imaging.

References and links

1. R. Alvarez-Román, A. Naik, Y. N. Kalia, H. Fessi, and R. H. Guy, "Visualization of skin penetration using confocal laser scanning microscopy," *Eur. J. Pharm. Biopharm.* **58**(2), 301–316 (2004).
2. R. Alvarez-Román, A. Naik, Y. N. Kalia, R. H. Guy, and H. Fessi, "Skin penetration and distribution of polymeric nanoparticles," *J. Control. Release* **99**(1), 53–62 (2004).
3. X. Wu, P. Griffin, G. J. Price, and R. H. Guy, "Preparation and in vitro evaluation of topical formulations based on polystyrene-poly-2-hydroxyl methacrylate nanoparticles," *Mol. Pharmacol.* **6**(5), 1449–1456 (2009).
4. A. V. Zvyagin, X. Zhao, A. Gierden, W. Sanchez, J. A. Ross, and M. S. Roberts, "Imaging of zinc oxide nanoparticle penetration in human skin in vitro and in vivo," *J. Biomed. Opt.* **13**(6), 064031 (2008).
5. J. Moger, B. D. Johnston, and C. R. Tyler, "Imaging metal oxide nanoparticles in biological structures with CARS microscopy," *Opt. Express* **16**(5), 3408–3419 (2008).
6. L. J. Mortensen, G. Oberdorster, A. P. Pentland, and L. A. DeLouise, "In vivo skin penetration of quantum dot nanoparticles in the murine model: the effect of UVR," *Nano Lett.* **8**(9), 2779–2787 (2008).
7. L. W. Zhang and N. A. Monteiro-Riviere, "Assessment of quantum dot penetration into intact, tape-stripped, abraded and flexed rat skin," *Skin Pharmacol. Appl.* **21**, 166–180 (2008).
8. N. V. Gopee, D. W. Roberts, P. Webb, C. R. Cozart, P. H. Siitonen, J. R. Latendresse, A. R. Warbitton, W. W. Yu, V. L. Colvin, N. J. Walker, and P. C. Howard, "Quantitative determination of skin penetration of PEG-coated

- CdSe quantum dots in dermabraded but not intact SKH-1 hairless mouse skin," *Toxicol. Sci.* **111**(1), 37–48 (2009).
9. S. Paliwal, G. K. Menon, and S. Mitragotri, "Low-frequency sonophoresis: ultrastructural basis for stratum corneum permeability assessed using quantum dots," *J. Invest. Dermatol.* **126**(5), 1095–1101 (2006).
 10. L. J. Mortensen, H. Zheng, R. Faulknor, A. De Benedetto, L. Beck, and L. A. DeLouise, "Increased in vivo skin penetration of quantum dots with UVR and in vitro quantum dot cytotoxicity," *Proc. SPIE* **7189**, 718919 (2009).
 11. J. Seto, B. Polat, R. Lopez, D. Blankshtein, and R. Langer, "Effects of ultrasound and sodium lauryl sulfate on the transdermal delivery of hydrophilic permeants: comparative in vitro studies with full-thickness and split-thickness pig and human skin," *J. Control. Release* **145**(1), 26–32 (2010).
 12. H. S. Choi, W. Liu, P. Misra, E. Tanaka, J. P. Zimmer, B. Itty Ipe, M. G. Bawendi, and J. V. Frangioni, "Renal clearance of quantum dots," *Nat. Biotechnol.* **25**(10), 1165–1170 (2007).
 13. J. A. Fitzpatrick, S. K. Andreko, L. A. Ernst, A. S. Waggoner, B. Ballou, and M. P. Bruchez, "Long-term persistence and spectral blue shifting of quantum dots in vivo," *Nano Lett.* **9**(7), 2736–2741 (2009).
 14. B. J. Marquis, S. A. Love, K. L. Braun, and C. L. Haynes, "Analytical methods to assess nanoparticle toxicity," *Analyst* **134**(3), 425–439 (2009).
 15. N. A. Lewinski, V. L. Colvin, and R. A. Drezek, "Cytotoxicity of nanoparticles," *Small* **4**(1), 26–49 (2008).
 16. P. Rivera Gil, G. Oberdörster, A. Elder, V. Puentes, and W. J. Parak, "Correlating physico-chemical with toxicological properties of nanoparticles: the present and the future," *ACS Nano* **4**(10), 5527–5531 (2010).
 17. M. J. Bartek, J. A. LaBudde, and H. I. Maibach, "Skin permeability in vivo: comparison in rat, rabbit, pig and man," *J. Invest. Dermatol.* **58**(3), 114–123 (1972).
 18. T. J. Franz, "Percutaneous absorption on the relevance of in vitro data," *J. Invest. Dermatol.* **64**(3), 190–195 (1975).
 19. R. L. Bronaugh and R. F. Stewart, "Methods for in vitro percutaneous absorption studies IV: The flow-through diffusion cell," *J. Pharm. Sci.* **74**(1), 64–67 (1985).
 20. X. Wu, G. J. Price, and R. H. Guy, "Disposition of nanoparticles and an associated lipophilic permeant following topical application to the skin," *Mol. Pharmaceutics* **6**(5), 1441–1448 (2009).
 21. R. F. Lopez, J. E. Seto, D. Blankshtein, and R. Langer, "Enhancing the transdermal delivery of rigid nanoparticles using the simultaneous application of ultrasound and sodium lauryl sulfate," *Biomaterials* **32**(3), 933–941 (2011).
 22. M. S. Roberts, M. J. Roberts, T. A. Robertson, W. Sanchez, C. Thörling, Y. Zou, X. Zhao, W. Becker, and A. V. Zvyagin, "In vitro and in vivo imaging of xenobiotic transport in human skin and in the rat liver," *J. Biophotonics* **1**(6), 478–493 (2008).
 23. D. K. Bird, A. L. Schneider, A. C. Watkinson, B. Finin, and T. A. Smith, "Navigating transdermal diffusion with multiphoton fluorescence lifetime imaging," *J. Microsc.* **230**, 61–69 (2008).
 24. T.-R. Kuo, C.-L. Wu, C.-T. Hsu, W. Lo, S.-J. Chiang, S.-J. Lin, C.-Y. Dong, and C.-C. Chen, "Chemical enhancer induced changes in the mechanisms of transdermal delivery of zinc oxide nanoparticles," *Biomaterials* **30**(16), 3002–3008 (2009).
 25. M. Kirillin, M. Shirmanova, M. Sirotkina, M. Bugrova, B. Khlebtsov, and E. Zagaynova, "Contrasting properties of gold nanoshells and titanium dioxide nanoparticles for optical coherence tomography imaging of skin: Monte Carlo simulations and in vivo study," *J. Biomed. Opt.* **14**(2), 021017 (2009).
 26. M. Sirotkina, M. Shirmanova, M. Bugrova, V. Elagin, P. Agrba, M. Kirillin, V. Kamensky, and E. Zagaynova, "Continuous optical coherence tomography monitoring of nanoparticles accumulation in biological tissues," *J. Nanopart. Res.* **13**(1), 283–291 (2010).
 27. X. He, K. Wang, and Z. Cheng, "In vivo near-infrared fluorescence imaging of cancer with nanoparticle-based probes," *WIREs Nanomed. Nanobiotechnol.* **2**(4), 349–366 (2010).
 28. H. S. Choi, B. Itty Ipe, P. Misra, J. H. Lee, M. G. Bawendi, and J. V. Frangioni, "Tissue- and organ-selective biodistribution of NIR fluorescent quantum dots," *Nano Lett.* **9**(6), 2354–2359 (2009).
 29. H. S. Choi, W. Liu, F. Liu, K. Nasr, P. Misra, M. G. Bawendi, and J. V. Frangioni, "Design considerations for tumour-targeted nanoparticles," *Nat. Nanotechnol.* **5**(1), 42–47 (2010).
 30. M. Rajadhyaksha, S. Gonzalez, J. Zavislan, R. R. Anderson, and R. Webb, "In vivo confocal scanning laser microscopy of human skin II: advances in instrumentation and comparison with histology," *J. Invest. Dermatol.* **113**, 293–303 (1999).
 31. Z. Wang, C. E. Glazowski, and J. M. Zavislan, "Modulation transfer function measurement of scanning reflectance microscopes," *J. Biomed. Opt.* **12**(5), 051802 (2007).
 32. S. Empedocles, R. Neuhauser, and M. Bawendi, "Three-dimensional orientation measurements of symmetric single chromophores using polarization microscopy," *Nature* **399**(6732), 126–130 (1999).
 33. M. J. van Gemert, S. L. Jacques, H. J. Sterenborg, and W. M. Star, "Skin optics," *IEEE Trans. Biomed. Eng.* **36**(12), 1146–1154 (1989).
 34. S. Nickell, M. Hermann, M. Essenpreis, T. J. Farrell, U. Krämer, and M. S. Patterson, "Anisotropy of light propagation in human skin," *Phys. Med. Biol.* **45**(10), 2873–2886 (2000).
 35. S. H. Tseng, A. Grant, and A. J. Durkin, "In vivo determination of skin near-infrared optical properties using diffuse optical spectroscopy," *J. Biomed. Opt.* **13**(1), 014016 (2008).

36. S. H. Tseng, P. Bargo, A. Durkin, and N. Kollias, "Chromophore concentrations, absorption and scattering properties of human skin in-vivo," *Opt. Express* **17**, 14599–14617 (2009).
37. C. K. Hayakawa, E. O. Potma, and V. Venugopalan, "Electric field Monte Carlo simulations of focal field distributions produced by tightly focused laser beams in tissues," *Biomed. Opt. Express* **2**, 278–290 (2011).
38. R. R. Anderson and J. A. Parrish, "The optics of human skin," *J. Invest. Dermatol.* **77**(1), 13–19 (1981).
39. C. R. Simpson, M. Kohl, M. Essenpreis, and M. Cope, "Near-infrared optical properties of ex vivo human skin and subcutaneous tissues measured using the Monte Carlo inversion technique," *Phys. Med. Biol.* **43**(9), 2465–2478 (1998).
40. C. A. Leatherdale, W.-K. Woo, F. V. Mikulec, and M. G. Bawendi, "On the absorption cross section of cdse nanocrystal quantum dots," *J. Phys. Chem. B* **106**(31), 7619–7622 (2002).
41. L. Cademartiri, E. Montanari, G. Calestani, A. Migliori, A. Guagliardi, and G. A. Ozin, "Size-dependent extinction coefficients of PbS quantum dots," *J. Am. Chem. Soc.* **128**(31), 10337–10346 (2006).
42. B.-R. Hyun, H. Chen, D. A. Rey, F. W. Wise, and C. A. Batt, "Near-infrared fluorescence imaging with water-soluble lead salt quantum dots," *J. Phys. Chem. B* **111**(20), 5726–5730 (2007).
43. S. Ravichandran, L. J. Mortensen, and L. A. DeLouise, "Quantification of human skin barrier function and susceptibility to quantum dot skin penetration," *Nanotoxicology* **Early Online**, 1–12 (2010).
44. T. Dutkiewicz and H. Tyras, "Skin absorption of toluene, styrene, and xylene by man," *Br. J. Ind. Med.* **25**(3), 243 (1968).
45. H. Tsuruta, "Percutaneous absorption of organic solvents. III. On the penetration rates of hydrophobic solvents through the excised rat skin," *Ind. Health* **20**(4), 335–345 (1982).
46. N. V. Gopee, D. W. Roberts, P. Webb, C. R. Cozart, P. H. Siitonen, A. R. Warbritton, W. W. Yu, V. L. Colvin, N. J. Walker, and P. C. Howard, "Migration of intradermally injected quantum dots to sentinel organs in mice," *Toxicol. Sci.* **98**(1), 249–257 (2007).
47. F. F. Larese, F. D'Agostin, M. Crosera, G. Adami, N. Renzi, M. Bovenzi, and G. Maina, "Human skin penetration of silver nanoparticles through intact and damaged skin," *Toxicology* **255**, 33–37 (2009).
48. B. Gulson, M. McCall, M. Korsch, L. Gomez, P. Casey, Y. Oytam, A. Taylor, M. McCulloch, J. Trotter, L. Kinsley, and G. Greenoak, "Small amounts of zinc from zinc oxide particles in sunscreens applied outdoors are absorbed through human skin," *Toxicol. Sci.* **118**(1), 140–149 (2010).

1. Introduction

The increasing presence of nanoparticles (NPs) in consumer products and technical applications has indicated a need to understand their interaction with the human system. To this end, a number of studies have investigated the ability of NPs to penetrate the skin. Most recent studies suggest that intact skin is an adequate barrier for hydrophilic NPs of polymeric [1–3], metal oxide [4, 5], and semiconductor quantum dots (QDs) [6–8]. However, when barrier is impaired there appears to be an increased ability for NPs to penetrate the skin and interact with the local cell types and the body system [6–11]. Since most NPs studied thus far are larger than the size threshold for renal filtration [12], studies have suggested their ability to remain in the body [13] and potentially to cause long terms problems in a variety of cell types and NP types [14–16].

The field of NP skin penetration is largely built on research into the percutaneous absorption of other substances. Evaluation of percutaneous absorption has been a subject of investigation for a number of years, and the field of transdermal drug delivery has encouraged the development of efficient detection systems for molecular targets, including analysis of acceptor solution in a static or flow-through diffusion cell, in vivo systemic distribution, histological analysis, and whole-tissue imaging in the skin [17–19]. Similarly, as interest in the diffusion of NPs through the skin has grown, so too has the technology that endeavors to understand these phenomenon. However, when attempting to evaluate toxicological effects of skin penetration, low frequency events may be important and so factors such as detection limits and the state of the nanoparticle (i.e. dissolved ions or intact NPs) in the skin become increasingly critical.

One of the most promising ways to address these problems is through development of novel imaging modalities. For imaging of NPs, the possible modalities depend on the physical characteristics of the NP. The most commonly implemented form of advanced microscopy is that of fluorescent confocal microscopy. Fluorescent confocal imaging provides advantages in the exclusion of defocused light using a pinhole, and therefore allows optical sectioning of samples.

Despite its ubiquity confocal microscopy is often relegated to analysis of histological samples in practice, but some examples of whole tissue microscopy have been reported. Richard Guy's group has been one of the pioneers in this area, using confocal microscopy to evaluate the skin penetration of a variety of fluorescent polymeric NPs [1–3, 20]. For example, a 2004 study by Alvarez-Roman et al. found that FITC labeled polystyrene NPs of 20 nm and 200 nm diameter were unable to penetrate porcine stratum corneum [1, 2]. For QDs, a class of hard semiconductor NPs, our research was unable to find appreciable skin penetration using green fluorescent QDs and whole tissue confocal microscopy [6]. Robert Langer's group has also used this technique to support reported increased skin penetration of QDs with sonophoresis and sodium lauryl sulfate treatment [21]. However, in all of these studies visible range whole tissue confocal microscopy is a minor supporting technique, since epidermal scattering and absorption limit the penetration depth of light, both in the acceptable laser excitation powers as well as the returned fluorescence. Multiphoton microscopy overcomes the excitation and average power limitations of visible range confocal microscopy by using femtosecond pulses of near-IR light at twice the excitation wavelength, thereby achieving greater imaging depth in the skin. The technique functions by 2-photon fluorescent excitation or second harmonic generation (SHG) of the target analyte, and has detected ZnO NPs using SHG [4, 22, 23]. One study has even been able to put the technique into practice and demonstrate an increased skin penetration of ZnO NPs with barrier disruption by chemical penetration enhancers [24]. These studies are significant, as ZnO is an important particle that is commonly used in topically applied sunscreens, but its commonly used dominant emission peak at 385 nm limits the detection depth achievable. To attempt to address these limitations, other techniques such as optical coherence tomography and coherent anti-stokes raman spectroscopy have been implemented, but little literature exists on their application in the skin [5, 25, 26].

Our work examines the potential of both a near-IR excitation source and a near-IR emitting QDs to evaluate whole tissue skin penetration of NPs. QDs are a category of NPs that have shown potential as a model for other hard insoluble metallic and metal oxide NPs, and are of primary interest in the electronics and biomedical research fields. They provide advantages in biomedical imaging due to their broad excitation band, high photobleaching threshold, ease of functionalization, and stability. However, no studies currently exist in the literature that utilize whole tissue microscopy to localize the penetration profiles of near-IR QDs through the skin. Additionally, despite work determining the whole-body distribution of functionalized near-IR QDs and targeting towards tumor tissues [27–29], we are unable to locate any studies that examine near-IR QD skin penetration profiles and the impact of skin barrier status on skin penetration using any techniques. Our system, reported herein, endeavors to overcome the limitations of visible range whole tissue microscopies by establishing a completely near-IR confocal microscopy system. We have developed an optimized near-IR excitation and emission confocal system that we have fully characterized and validated to allow the imaging of QDs through the epidermis and demonstrated its sensitivity through an ex vivo human skin sample. Our system shows potential to allow the evaluation of skin penetration profiles for near-IR QDs and increase understanding of NP penetration mechanisms and translocation through skin and other tissues.

2. Materials and methods

2.1. Instrumentation

For these experiments, a Lucid VivaScopeTM reflectance confocal microscope prototype (Lucid, Inc., Rochester, NY) was rebuilt to allow imaging using both 660 nm and 785 nm laser wavelengths. Our schematic highlights the important components of the system (Fig. 1). The inclusion of a 664 nm long pass filter (LP02-664RS, Semrock Corp., Rochester, NY) allows the

detection of QDs while excluding the excitation wavelength. To maximize sensitivity, lenses with a visible to near-IR coating (VIS-NIR coating, Edmund Optics, Barrington, NJ), fold mirrors with a protected silver coating (ER.2, Newport Corp., Irvine, CA), an enhanced aluminum polygon (07 coating, Lincoln Laser Corp., Phoenix, AZ), a dichroic mirror to combine beam paths (LaserMUX 659, Semrock Corp., Rochester, NY), and a long wavelength silicon avalanche photo-diode (APD) detector (C5460/S8890 custom module, Hamamatsu Corp., Bridgewater, NJ) were selected as determined by the manufacturer's specifications. Scanning, timing, and collection systems used were based on designs reported previously [30]. The 660 nm and 785 nm illuminating laser beams were scanned across the sample by the polygon and galvanometric mirrors and relayed into the 30x 0.9-NA water immersion objective (Photon Gear, Rochester, New York), with 5x magnification. The reflected and fluorescently excited light was then relayed back out through the pinhole (138 μm diameter) and to the APD. The effective field of view for our 10 bit 976x980 pixel image is 0.319 mm x 0.323 mm, yielding a pixel pitch of 0.327 μm x 0.329 μm per pixel. Axial scanning is performed using a micrometer to move the stage in the z-direction. To determine system resolution, a technique developed in previous studies to achieve Nyquist sampling and a smooth modulation transfer function on a single edge target was used [31]. Using this technique, we found lateral and axial resolutions of 0.6 ± 0.02 μm and 4.8 ± 0.15 μm for the 660 nm laser and 0.8 ± 0.03 μm and 2.4 ± 0.08 μm for the 785 nm laser. Lower axial resolution observed with the 660 nm laser is due to the apochromatic coatings in the objective, the larger effective pinhole size for the 660 nm laser, and relative beam quality of the laser source.

2.2. Estimation of sensitivity

The performance of a fluorescence imaging system in the skin depends on a number of factors. Here we will account for the known optical parameters in order to reach a prediction of sensitivity. Benchmarking sensitivity measurements by theoretical approximation of expected signal is an important task when approaching an imaging problem where an unknown concentration of a substance in a biological milieu is the analyte. To achieve this for our system, the performance of each system component is measured or estimated from manufacturer specification and the reflectivity or transmittivity multiplied together at the 660 nm and 785 nm wavelengths. As such, the expression that includes the lens entry and exit transmittivity ($T_{L\lambda_i}$), the mirror reflectivities ($R_{M\lambda_i}$), the dichroic mirror reflectivity ($R_{D\lambda_i}$), the galvo reflectivity ($R_{G\lambda_i}$), the polygon reflectivity ($R_{P\lambda_i}$), the polarizing beamsplitter surface transmittivity (T_{PB}), the polarizing beamsplitter internal surface reflectivity (R_{PB}), the objective pupil area (A_P), the magnified beam area at the pupil (A_B), and the objective transmittivity (T_{Ob}) provides an estimate of the transmittivity between the laser source and the focal plane (Eq. (1)). To condense the descriptive equation, each component factor is raised to the power of its number of occurrences (lenses have an entry and an exit value) in the beam path as depicted (Fig. 1).

$$T_{SFP\lambda_i} = (T_{L\lambda_i})^8 (R_{M\lambda_i})^4 (R_{D\lambda_i}) (R_{G\lambda_i}) (R_{P\lambda_i}) (T_{PB})^2 (R_{PB}) \left(\frac{A_P}{A_B} \right) (T_{Ob}) \quad (1)$$

To test the accuracy of our estimates, we compared the predicted system throughput with the actual laser power throughput for 660 nm in the system path up to the focal plane. By testing at several powers, we found an average power throughput at 660 nm of 18% before the objective, as compared with a prediction of 19%. The minor disparity between our predicted and experimental values may be due to some polarization rejection of the laser source. The theoretical objective transmittivity is unreported by the manufacturer across our range of wavelengths, but we found experimentally that the beam at 660 nm passed 17% of the laser power present. These values are used in subsequent power approximations.

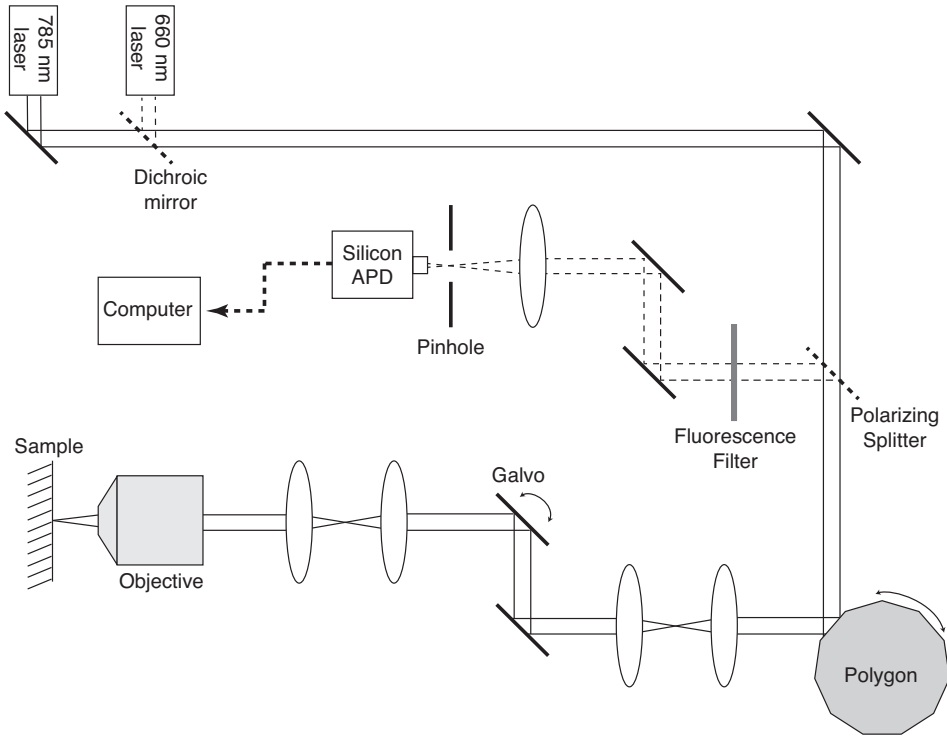


Fig. 1. The basic optical design for the system used in these experiments. Reflectance (785 nm) and fluorescence (660 nm excitation) sources are pumped into a laser scanning confocal microscopy system.

To estimate the ability of our system to measure light that returns to the detector from a fluorescent probe, the noise equivalent power (NEP) of the detector is used. NEP is a commonly quoted efficiency metric that describes the needed amount of power to equal the inherent detector noise. For our detector, the manufacturer specified NEP is $0.15 \text{ pW}/\sqrt{\text{Hz}}$ at the optimal sensitivity wavelength of 940 nm normalized to a 1 Hz bandwidth modulation. The NEP is inversely proportional to the photo sensitivity, whose wavelength dependent characteristics are reported by the manufacturer. Thus, a wavelength distributed NEP response with relative values across the active range of our system ($NEP_{Detector\lambda_i}$) can be estimated. This value must then be transformed for the bandwidth used in our system, which requires division by the square root of the dwell time in seconds (t_{dwell}). The noise equivalent power level generated at the focal plane at a given wavelength ($NEP_{FPD\lambda_i}$) then scales by the component efficiency between the focal plane and the detector, as depicted in the system schematic (Fig. 1), which increases the amount of power that QDs in the focal plane must generate to achieve NEP.

$$NEP_{FPD\lambda_i} = (NEP_{Detector\lambda_i}) \left[(\sqrt{t_{dwell}}) (T_{Ob}) (T_{L\lambda_i})^{10} (R_{M\lambda_i})^3 (R_{G\lambda_i}) (R_{P\lambda_i}) (T_{PB})^2 \left(\frac{1}{2} R_{PB}\right) \right]^{-1} \quad (2)$$

The objective solid angle (Ω) is another important factor in the microscope that decreases

the portion of QD signal relayed through the system. QDs emit light isotropically in a classical dipole pattern [32], and we assume random orientation of the QDs in the focal plane, which results in a uniform spherical average emission ($\Omega_{sphere} = 4\pi$). However, the collection is limited by the numerical aperture of the objective (NA) and the refractive index of the medium (RI), and scales the collected QD fluorescence by the proportion of the objective solid angle to the whole angle of the emission sphere.

$$\Omega = 2\pi \left(1 - \cos \left(\arcsin \left(\frac{NA}{RI} \right) \right) \right) \quad (3)$$

Since the system and detector performance is strongly dependent on wavelength, a realistic representation of the QD emission peak is used. For this purpose, the manufacturer reported spectroscopic profile of our QDs results in a semi-Gaussian distribution with a FWHM of 200 nm (Fig. 2(A)). This normalized profile is represented by the term $I_{QD\lambda_i}$. For a specified peak wavelength, the expression is numerically integrated (25 nm step size) from 200 nm to 1600 nm using the corresponding values for components to yield the NEP needed at the focal plane.

$$NEP_{QD} = \frac{4\pi}{\Omega} \int_{\lambda_i=200}^{\lambda_i=1600} (I_{QD\lambda_i}) (NEP_{FPD\lambda_i}) d\lambda_i \quad (4)$$

Additionally, since we wish to ultimately allow the imaging of QDs through epidermal tissue, the expression can be expanded to include the non-reduced tissue scattering coefficients ($\mu_{s\lambda_i}$), calculated from literature values for the reduced scattering coefficient ($\mu'_{s\lambda_i}$) and the anisotropy factor (g) in similarly sourced human skin [33–38], and absorption coefficients ($\mu_{a\lambda_i}$) from the literature for ex vivo human tissue [39]. The non-reduced scattering coefficients were selected based on wavefront error Strehl ratio comparison to scattering coefficients, which found that the reduced scattering coefficients are too low to predict the proper Strehl effect, and suggested that non-reduced scattering coefficients are on the right order. A fixed depth (z) of 100 μm (Eq. (5)) was selected to represent the average thickness of human epidermis and provides an estimate of imaging ability through human epidermis.

$$NEP_{QD-epi} = \frac{4\pi}{\Omega} \int_{\lambda_i=200}^{\lambda_i=1600} (I_{QD\lambda_i}) (NEP_{FPD\lambda_i}) \left(e^{-z(\mu_{s\lambda_i} + \mu_{a\lambda_i})} \right) d\lambda_i \quad (5)$$

The next phase of the model is the determination of optimal laser wavelength and the laser power needed to achieve NEP by exciting the QDs with that wavelength. We first selected a QD sample with a known concentration and a peak at the optimal wavelength determined using our calculations, and measured the absorbance (Fig. 2(A)). The Beer-Lambert law can then be used to determine the extinction coefficient (ϵ_λ) at each wavelength, and this value substituted into the equation established for use in CdSe/ZnS QDs [40] and validated in PbS QDs [41] for a single QD absorption cross section (C_{abs} , cm^{-2})

$$C_{abs} = \frac{2303\epsilon_\lambda}{N_A} \quad (6)$$

where N_A is Avogadro's number. To determine the laser power needed to achieve NEP at the detector, the estimated QD power generation (Fig. 3) determined in Eq. (5) is transformed into units of $W\text{cm}^{-2}$ using the absorption cross section (C_{abs}). For this portion of our estimate, the QDs are assumed to reside in the beam waist with a uniform illumination. With the inclusion of the manufacturer's specified QD quantum yield (QY) and proportion of fluorescence collected in the dwell time, the laser fluence needed at the focal plane can be calculated. The Evident

Technologies PbS QDs used in our experiments had a specified QY of about 40%. The collected light is reduced by the proportion of QD fluorescence that is released during the dwell time, which is determined by the fluorescence lifetime reported in the literature for the PbS QDs used in our experiments [42]. Since the normal excitation lag time is on the order of picoseconds, it is unnecessary to include this in the calculation. Fluorescence emission is commonly modeled for QDs to follow an exponential decay of the formula $e^{-t/\tau}$ where τ is the fluorescence decay, but for the Evident Technologies PbS QDs a two component fit of the form $A_1 \exp(-t/\tau_1) + A_2 \exp(-t/\tau_2)$ has been found to be more descriptive [42]. For our samples, the established two component values from Hyun et al. will be implemented, and so the proportion of signal collected becomes the integral of the decay curve at the pixel dwell time divided by the integral of the decay curve as $t \rightarrow \infty$, which we will refer to as I_{DT} (0.24 in this case). The radius of the Airy Disk for the laser is used to estimate the effective focused laser spot area, a function of the objective numerical aperture (NA) and the laser wavelength (λ_L), to correct for laser power density, yielding a laser power input distribution in units of $W\text{ cm}^{-2}$. Since the absorption cross section of a QD is much smaller than the diffraction limited beam waist focal spot, the area ratio is an important factor in determining the relative amount of laser power in Watts needed at the focal plane (NEP_{LFP}) to achieve detector NEP.

$$NEP_{LFP} = (NEP_{QD}) \left(\pi \left(\frac{0.61\lambda_L}{NA} \right)^2 \right) [(QY)(I_{DT})(C_{abs})]^{-1} \quad (7)$$

To determine the power needed to achieve NEP at the laser source, the NEP_{LFP} (Eq. (7)) is then divided by the power loss from the focal plane to the source as described above (Eq. (1)).

$$NEP_{Laser} = (NEP_{LFP}) (T_{SFP\lambda_i})^{-1} \quad (8)$$

To determine the impact of imaging through the skin, the NEP_{QD-epi} term expressed in Eq. (5) is then substituted into Eq. (7) to yield the noise equivalent power that . This value is a best-case scenario, since the Strehl ratio of the beam decreases with increasing imaging depth in tissue.

$$NEP_{LFP-epi} = (NEP_{QD-epi}) \left(\pi \left(\frac{0.61\lambda_L}{NA} \right)^2 \right) [(QY)(I_{DT})(C_{abs})]^{-1} \quad (9)$$

The expression can be finalized in the same form as Eq. (8) with the additional inclusion of skin scattering ($\mu_{s\lambda_i}$) and absorption ($\mu_{a\lambda_i}$) as discussed above through 100 μm of epidermis (z) to yield an increase in the needed laser power.

$$NEP_{Laser-epi} = (NEP_{LFP-epi}) (T_{SFP\lambda_i})^{-1} \left(e^{z(\mu_{s\lambda_i} + \mu_{a\lambda_i})} \right) \quad (10)$$

2.3. Quantum dot imaging

Near-IR QDs with a lead-sulfide core and an emission peak of 900 nm in toluene were purchased from Evident Technologies Inc. (Albany, New York) for our imaging studies. The absorbance profile and quantum yields were measured to ensure precise prediction of the system response to the QDs (Fig. 2(A)). To allow the imaging of QDs in a vertical configuration in solution, PDMS microwells (100 μm diameter by 10 μm deep) were filled with QDs at a series of concentrations and clamped between a glass coverslip and a microscope slide (Figs. 2(B) and 2(C)). This procedure excluded the QD solution from the surrounding areas and allowed background signal to be collected in the same frame as the QD signal and separated using signal processing in Matlab (Fig. 2(D)). Before each imaging session, the laser power was calibrated

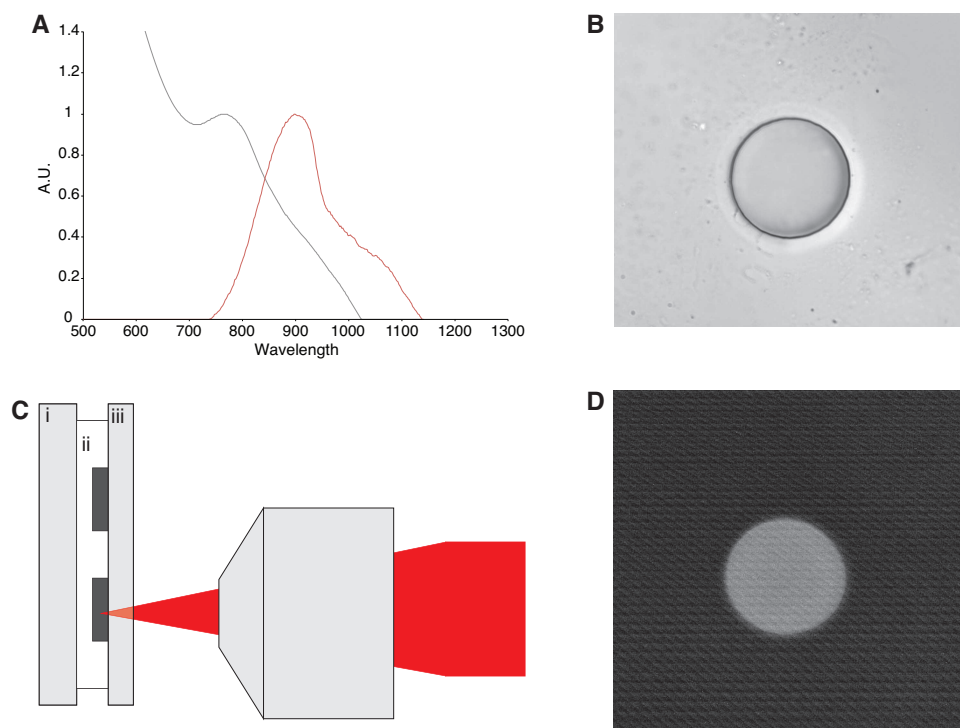


Fig. 2. Pictorial representation of an example normalized emission and absorbance curves (A) for the QDs used in these experiments. To enable imaging in the upright position, the PDMS microwells (B) of $100\ \mu\text{m}$ diameter and $10\ \mu\text{m}$ depth are filled with QDs and clamped as shown (C). Clamping the QD filled PDMS microwells (ii) between coverglass (iii) and a microscope slide (i) allows the imaging of a filled well. The QD signal ($\lambda_{\text{max}}=900\ \text{nm}$) can quite clearly be separated from the PDMS well.

to ensure accurate measurements. For imaging through a separated epidermis, the same setup is used with the addition of an ex vivo human epidermis between the PDMS microwells and the coverslip that we separated as described below.

2.4. Skin preparation

Our ex vivo human skin epidermis samples were obtained fresh from de-identified healthy adult donors following abdominoplasty or mammoplasty (Strong and Highland Hospitals, University of Rochester, NY), and stored at 4°C . Usage was approved by the University of Rochester Research Subjects Review Board. Within 6 hours of the surgical procedure, skin samples were rinsed with sterile 1x phosphate buffered saline (PBS), treated with 0.4 mL fungizone (Invitrogen) in 500 mL sterile 1x PBS for 10 min, and rinsed again thoroughly with 1x PBS. To allow the diffusion of our epidermal separating agent, subcutaneous fat was removed and the dermis thinned. The skin samples were then transferred to fresh 100 mm sterile tissue culture plates with gauze and incubated overnight at room temperature in 12 mL of 0.25% Dispase (Gibco Inc.) in a sterile cell culture hood with the stratum corneum exposed to the air. The epidermis was then separated from the dermis using tweezers and used for imaging immediately. To demonstrate instrument proof of principle in skin, $30\ \mu\text{L}$ of $10\ \mu\text{M}$ PbS QDs in toluene were

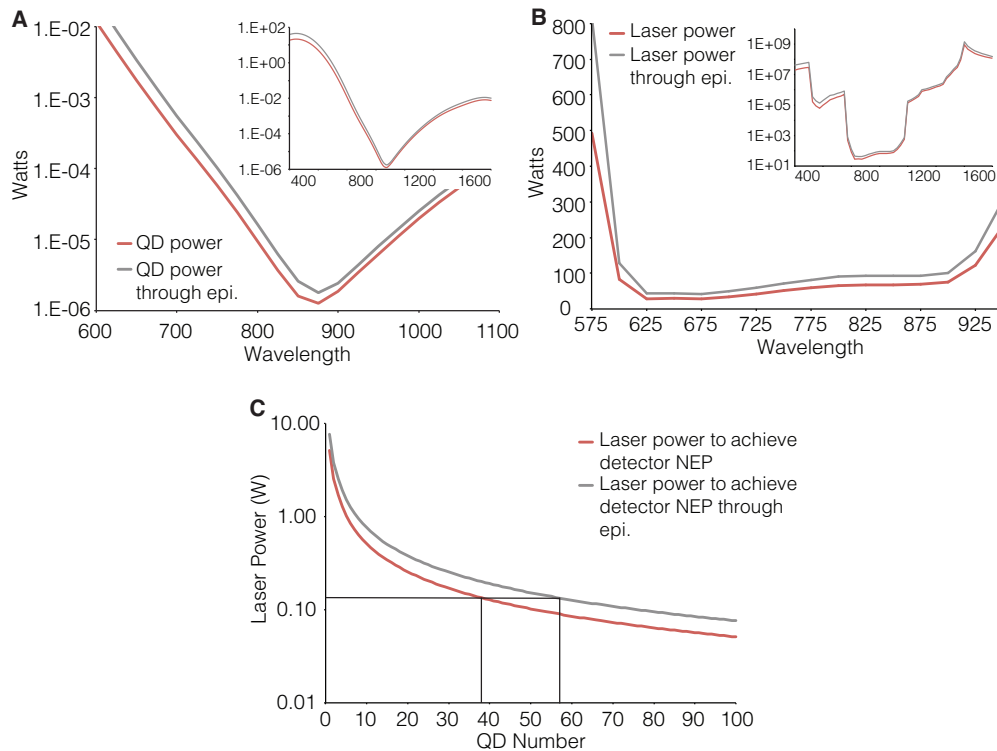


Fig. 3. Estimation of the power needed to be generated by QDs in the focal plane (A). The noise equivalent power (NEP) for the detector is scaled by the peak width of the QDs, the collection angle, and the system components. A clear minimum is observable in the ~ 900 nm wavelength emission peak range. Using the measured absorbance to estimate the absorption cross section then allows the minimum laser power needed to achieve NEP on a single QD (note: in practice this is limited by blinking) at a range of laser wavelengths, and it is observed that there is a power minimum at the 600-700 nm wavelength range (B), for which a 660 nm laser line was chosen. When the power limitations of our excitation source is included, the system response to a range of QD concentrations is able to be estimated (C).

applied to full thickness ex vivo human skin tape stripped (20x, Scotch 3M 3750 clear packing tape, USA) as described previously, [43] incubated for 24 hours with skin viability maintained by sitting on a KGM-SF (Gibco Inc.) soaked gauze pad with the stratum corneum exposed to the air, and used for imaging immediately thereafter.

3. Results and discussion

3.1. Sensitivity estimates

The predictions of system performance described above are useful in the estimation of anticipated sensitivity and determination of realistic limits for a given technique. With implementation for our detector and model QD emission distribution, the minimum NEPs calculated using Eq. (4) for QDs alone and Eq. (5) for QDs through $100 \mu\text{m}$ epidermis yield NEP minimums at 875 nm peak QD emission (Fig. 3(A)). This optimal value is close to that of the detector sensitivity, but the steep falloff of the detector (1100 nm cutoff) and the 200 nm FWHM of

the QDs push the detection values to slightly shorter wavelengths. Across the full wavelength range of our system, necessary power to achieve detector NEP ranges over 5 orders of magnitude (Fig. 3(A) inset). When an absorbance curve for QDs of this peak emission is converted to absorption cross section and included with the losses from objective solid angle, focal spot size, and system components, the resultant power needed to achieve NEP for a single QD can be estimated using Eq. (8) for QDs alone and Eq. (10) for QDs through 100 μm epidermis (Fig. 3(B)). We plot the value from 200 nm to 1600 nm, and find a clear minimum power needed to achieve detector NEP in the range of 600-700 nm (Fig. 3(B)). Thus, a laser line of 660 nm wavelength is selected. Our estimates suggest that the necessary laser power to observe a single QD is 5 Watts, with 7.3 Watts needed to detect a single QD below the thickness of a human epidermis. Such a high laser power is problematic due to cost, safety concerns, and destruction of the tissue sample. However, single fluorophore imaging is not vital to the goals of whole tissue skin penetration imaging and is not commonly achieved in other techniques. To provide an estimation of the minimum number of QDs in the focal plane needed to achieve NEP with varying laser power, Eq. (10) is divided by the number of QDs in the image plane for a given laser wavelength and plotted (Fig. 3(C)). The graph demonstrates that our laser currently in use (135 mW at 660 nm) provides greater than NEP signal with 38 QDs in the focal plane, and 57 QDs in the focal plane through 100 μm epidermis. If these values are normalized to the experimentally determined lateral resolution (0.59 μm at 660 nm) the diffraction limited spot size, sensitivities of approximately 5.7 fmol/cm^2 of QDs on the slide and 8.7 fmol/cm^2 QDs through 100 μm epidermis are achievable. The total applied dose in our previous QD skin penetration studies has been on the order of $\sim 3 \text{ pmol}/\text{cm}^2$, which suggests that our microscope will be able to detect as little as 0.2% of the applied dose on glass and 0.3% of the applied dose through 100 μm epidermis [6, 10]. If our laser power is increased to 1.5 W at the source (around 40 mW at the sample surface), a value that is achievable using a krypton ion laser, the number of QDs in the beam waist needed to reach NEP drops to 4 on glass and 6 through 100 μm epidermis, which corresponds to 0.61 fmol/cm^2 on glass or 0.92 fmol/cm^2 through 100 μm epidermis. These values correspond to 0.02% and 0.03% of the applied dose, respectively. Direct comparison to existing techniques is challenging, as few studies define their system sensitivities in the same fashion. However, our predicted sensitivity establishes the viability of whole tissue confocal microscopy in the near-IR as a technique with the potential to provide valuable information about permeation of substances through the epidermis with sub-cellular level lateral and axial resolution

3.2. Experimental validation and model comparison

To determine whether the system in practice holds up to its theoretical predictions, measurements of fluorescence intensity from QDs at various concentrations have been executed. As described in the materials and methods section, we suspended various concentrations of QDs in PDMS microwells clamped tightly between the coverslip and a microscope slide. The presence of 100 μm diameter microwells enables the background to be calculated from the same image as the QD signal, allowing for a facile representation of signal to noise within a sample. Each experiment was averaged over 6 different microwells at each concentration, and the curve repeated at 3 laser power levels (1.6 mW, 2.4 mW, and 3.9 mW at the focal plane, data not shown). In the high laser power case (3.9 mW at the focal plane), the signal gained from the QDs is distinguishable from background down to a concentration as low as 0.1 μM , and increases linearly over two orders of magnitude to a concentration of 10.0 μM (Fig. 4). When the QDs are imaged through separated human epidermis, there is a substantial decrease in the signal intensity across a range of concentrations, with the lowest detectable concentration of QDs at 2.0 μM . The imaging of a known concentration of a fluorescent probe to determine its

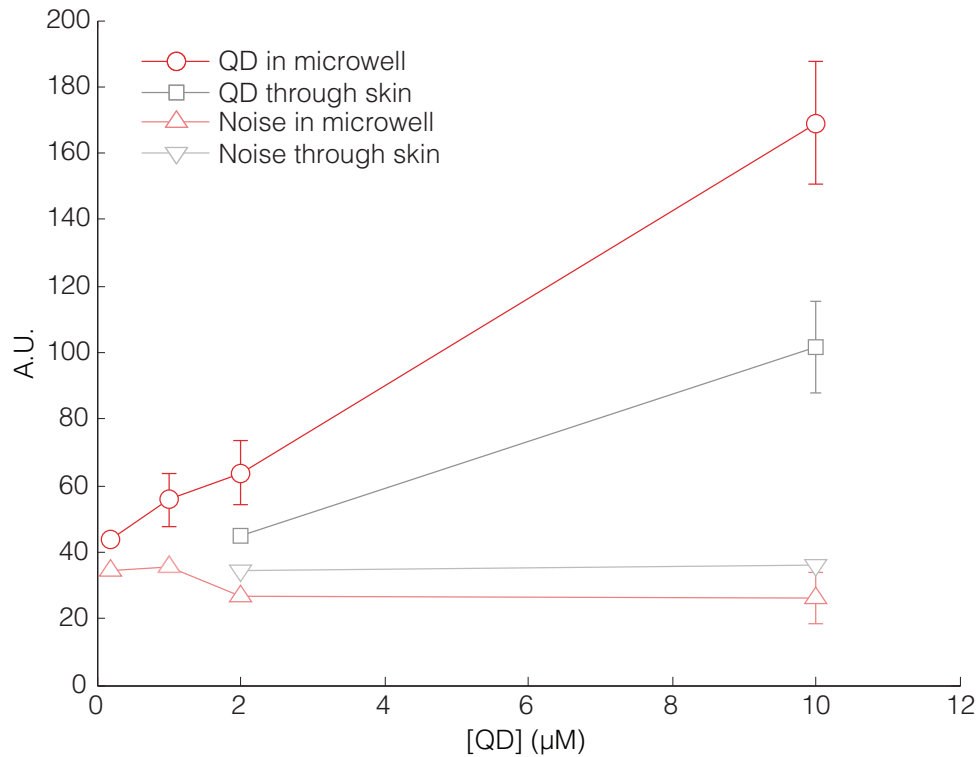


Fig. 4. Signal response of system to QDs across a range of concentrations in the microwell and through $\sim 100 \mu\text{m}$ separated human epidermis with a laser power of 3.9 mW at the focal plane. Background noise is also plotted, and is calculated from the same frames as the signal.

limit of detection is an important task when attempting to determine the ability of the a system to detect an unknown concentration of the probe in a tissue sample. Our technique of placing a known concentration of QDs behind approximately $100 \mu\text{m}$ of human epidermis allows for an accurate determination of the lower limit of detection in our system in practice, with the exception of scattering that would occur from apical QDs residing in the upper layers of the epidermis.

In order to compare our results to varied concentrations of QDs to our predictions, it is necessary to determine the predicted response to the number of QDs in a volume rather than the previously described area calculation. To do so, the number of QDs detected are scaled to the focal volume as determined by the lateral resolution ($0.59 \mu\text{m}$) and axial resolution ($4.75 \mu\text{m}$) of our system at 660 nm in practice. When plotted over the range of concentrations tested, the predictive measure matches well to experimental data (Fig. 5). For QDs imaged in the microwell alone and through human epidermis, our experimental fluorescent intensities matched expected values at low concentrations, but did not attain predicted intensity at higher concentrations. This may be caused by the assumption of uniform excitation efficiency of QDs in the focal plane, and the higher deviation from the model present when imaging through human epidermis may suggest a limit of epidermal scattering estimation or greater thickness of ex vivo separated epidermal tissue than expected. Differences are relatively minor at all tested QD concentrations. These values suggest that our system is operating at a near-ideal efficiency,

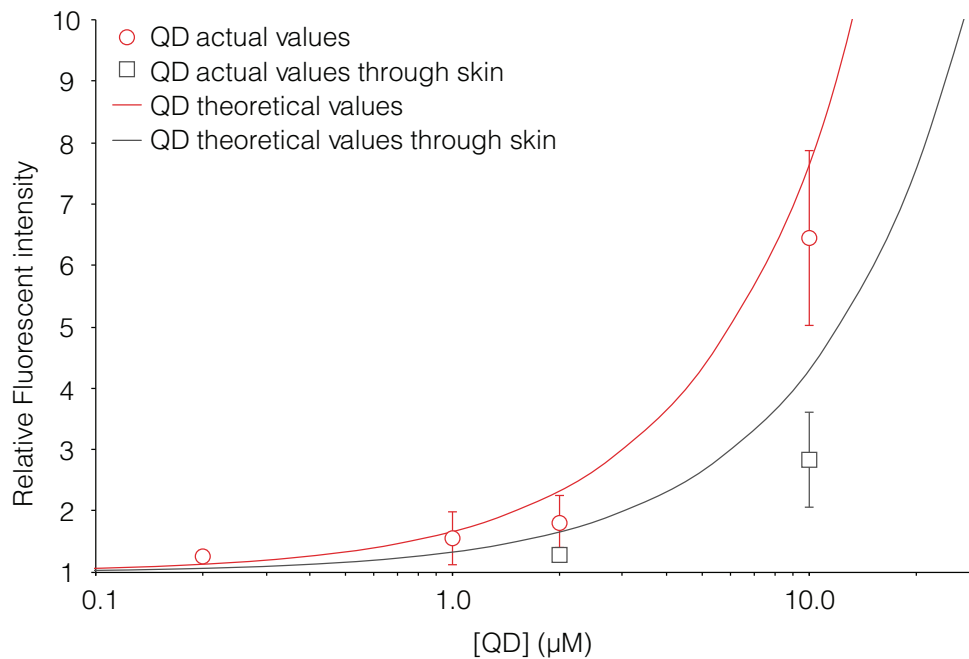


Fig. 5. The behavior of the experimental data follows the model. The improved theoretical sensitivity is expected, as we use idealized versions of the laser beams, QDs, and other components as well as scattering and absorption coefficients from the literature.

and inform a prediction of the ultimate limit of our sensitivity in practice.

3.3. QD skin penetration

Demonstration and calibration of the imaging system using QDs in microwells through separated epidermis nominally verified the predicted system performance. The next step is execution of skin penetration evaluation using topically applied QDs. To this end, QDs at stock concentration were applied to the skin in their toluene vehicle. Toluene is known to penetrate mammalian skin in high levels [44,45], and a 24 hour application procedure of QDs in organic solvent with additional barrier disruption through mechanical tape-stripping disruption provides an experimental model for potential incidental exposure to QDs in the workplace through damaged skin. Results find that skin images from the reflectance channel are strongly degraded even close to the surface of the skin (Fig. 6(A)), but cellular borders can still be observed (red arrows). QD fluorescence evaluation yields a strong signal (Fig. 6(B)) that can be traced into the tissue depth (Fig. 6(C)). A much slower drop-off in signal is clear versus the reflectance in depth, and when the ratio of these numbers is determined, the effective flux rate is plotted. Additional noise is present when imaging deeper in the tissue, but the curve suggests partitioning of the toluene-containing QDs at the stratum corneum/epidermal transition and a steady diffusive release into the epidermis. When the QD fluorescence and skin reflectance profiles are averaged over 6 locations in the skin (Fig. 6(D)), a consistent presence of QDs into the epidermis is clear, confirming the ability of our system to evaluate the skin penetration of QDs under relevant experimental conditions.

Since fluorescence is one of the key mechanisms that has been used to evaluate the skin penetration of NPs, understanding the technical limitations of evaluation techniques has important

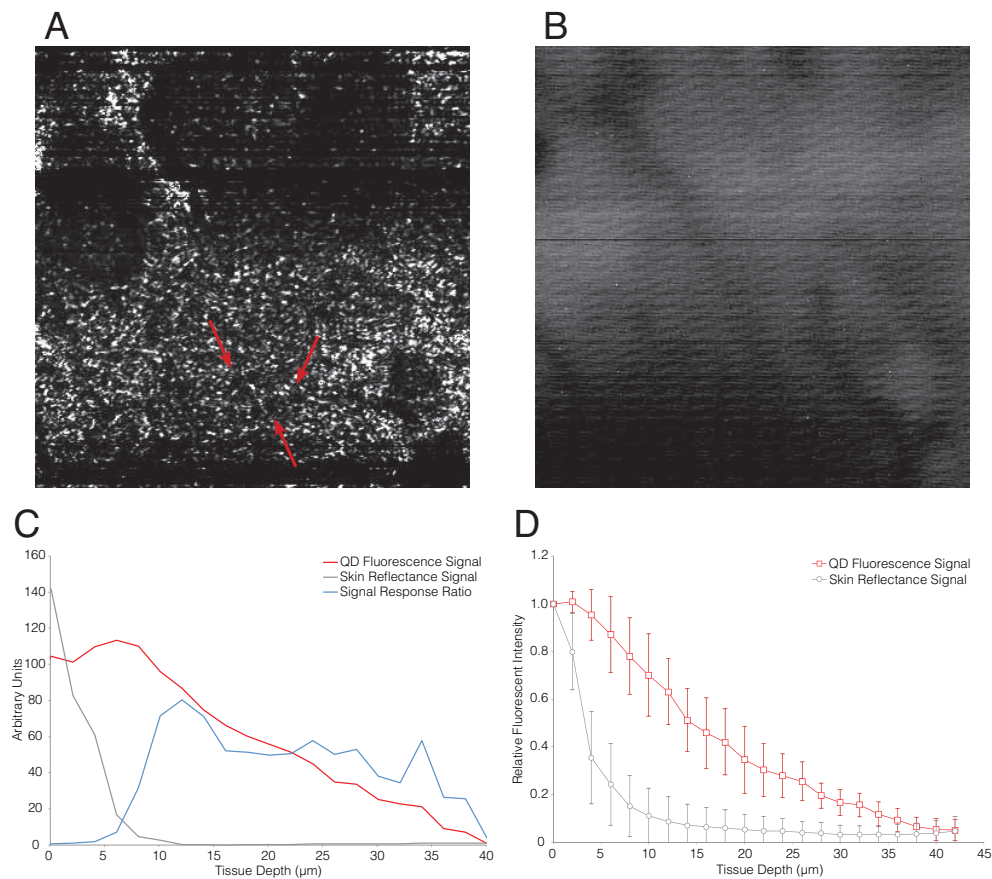


Fig. 6. Skin penetration of 900 nm peak emission PbS QDs in toluene. The reflectance signal close to the surface of the skin is degraded by the highly scattering QDs and toluene barrier disruption (A). However, some cell borders can still be resolved (arrows). The QDs provide a strong fluorescence signal at the same plane (B). When these profiles are plotted, a clear permeation of QDs into the epidermis is observable relative to the collected reflectance signal (C). The ratio of these values at each dose provides a steady-state flux curve determination, whose shape suggests that there is some partitioning of the toluene solvated QDs at the stratum corneum/epidermal junction with a steady release through the epidermis thereafter (C). The average of 6 measurement locations yields a curve exhibiting the average permeation of PbS QDs into the epidermis (D).

real-world implications in the application of results to assess risk and potential systemic toxicology. Noticeably lacking from all but the most rigorous of publications is an estimation of the minimum number of NPs that must be present to be detectable, and none that we have been able to find utilize fluorescence microscopy except as a supporting technique. In fact, only one study that we are currently aware of has been able to use whole tissue microscopy to determine a skin penetration profile of NPs. Kuo et al. have used second harmonic generation with multiphoton microscopy to find a change in the penetration profiles of ZnO NPs with various chemical penetration enhancing agents [24]. Their studies suggest that the treatment of skin with acetone, oleic acid, and a mixture of both is able to increase the collection of ZnO NPs in the stratum corneum and their diffusion through the epidermis. Use of SHG enables the distinction of NPs from released ions, an advantage that it shares with fluorescence. Despite this important advancement in the usage of whole tissue microscopy as a primary skin penetration evaluation technique, the authors did not address their ultimate sensitivity. To find published articles that examine the ultimate sensitivity of their techniques, more overtly quantitative techniques based around mass spectroscopy must be considered. Research by Gopee et al. has investigated the penetration of QDs through intact and damaged murine skin in vivo, and used the analysis of Cd in distal organs (liver and lymph nodes) to evaluate skin penetration of a total dose of 47 *pmol* QDs ($\sim 18 \text{ pmol/cm}^2$) [8]. Their study provides the limit of detection and the limit of quantification for their technique, but suffers due to the necessity of a large portion of QDs to penetrate the skin in order to achieve appreciable collection in the distal organs over background, with the first detectable difference in barrier defect occurring after 2% of the applied dose collected in the liver. In a previous study they injected QDs subcutally- mimicking the penetration of 100% of an applied dose (48 *pmol* QDs)- and found only 6% of the applied dose in the liver and 1% in the regional draining lymph nodes [46]. Hence, the liver collection levels required for their skin penetration study suggests that skin barrier disruption must allow 33% ($\sim 6 \text{ pmol/cm}^2$ QDs) of the applied dose to penetrate to a subcutal level for detection. This value is well within the ability of our system to evaluate. Recent work by Lopez et al. has studied the ability of sodium lauryl sulfate (SLS) and ultrasound to synergistically impact barrier function against QDs [21]. A very small but quantifiable percentage of the applied QDs with a total dose of 1 μmol QDs ($\sim 564.9 \text{ nmol/cm}^2$) were found to penetrate intact epidermis (0.006%-0.078% of the applied dose, or $\sim 33.9\text{-}440.7 \text{ pmol/cm}^2$ QDs) by mass spectroscopy on mechanically separated and cleaned dermis. These values are within the sensitivity limits of our system. In fact, the suggested pathway for their observed QD penetration is via lacunar imperfections of approximately 48 nm diameter and covering 0.44% of the skin surface area, as discussed in previous work by Mitragotri's group [9]. If it is assumed that the majority of QD skin penetration occurs through these pathways, then it can be estimated that the localized penetration channels allow 1.36%-17.73% ($\sim 7.7\text{-}100.2 \text{ nmol/cm}^2$) of the applied dose to pass, which is well within the detection limit of our system, and their ultrasound/SLS treatment increases the penetration of QDs into the dermis to levels of 80%- 99% of the applied dose. The limit of detection and quantification was calculated in a similar manner to that of Gopee et al., but baseline level of Cd observed in the dermal samples with no QD application was not reported. Whole tissue visible range confocal microscopy of the separated dermal samples supported their mass spectroscopy findings, with rare occurrences of localized spots of relatively high QD concentration, but was not used to establish a diffusion gradient. When considering mass spectroscopy based studies a major caveat must be noted, which is that the technique is unable to distinguish between the penetration of intact NPs or dissolved ions. With an acute application dose of ZnS-capped QDs this is not a major concern, but may be an important factor with other types of NPs, such as silver or ZnO NPs [47, 48]. The sensitivity evaluation of our system and practical application for imaging through human epidermis provides a distinct advantage for future studies to de-

termine the impact of skin barrier disruption on NP skin penetration and establish a model to understand the penetration of nanoparticulate substances.

4. Conclusions

The evaluation of NP skin penetration, either to determine risk factors or provide targeted delivery is an important area that has far-reaching clinical and toxicological implications. Our development of a whole tissue confocal imaging system in the near-IR range is a promising technique that exhibits great potential to address some previous limitations in the field, and help to complement existing state of the art whole tissue imaging techniques. We have optimized and characterized our reflectance and fluorescence confocal system performance and found the ability to image QDs in a controlled fashion through ex vivo human epidermis, with sensitivity surpassing 0.3% of our applied dose, and implemented it to detect QDs penetrating the skin in an ex vivo barrier disrupted model. Application-optimized system design and thorough testing enables greater confidence in imaging results and has the potential to expedite the evaluation of NP formulations and skin barrier alterations. With the movement of imaging modalities into the near-IR, a well characterized system can provide increased sensitivity and detection depth for an improved understanding of NP skin permeability.

Acknowledgments

We would like to acknowledge Ut-Binh Giang for her gift of the PDMS microwells, Lucid Inc. for their donation of the microscope prototype, and Chris Evans from the lab of Todd Krauss for his gift of near-IR lead-based QDs. This work was supported by the National Science Foundation (CBET 0837891) and the National Institute of Health (NIDA K25AI060884). Support for the multi-wavelength confocal microscope used in this research was provided by the National Institutes of Health (NCI 5R42CA110226) and New York State Office of Science, Technology and Academic Research (TTIP C020027).